Journal of Materials Science: Materials in Electronics (2020) 31:12455–12466
https://doi.org/10.1007/s10854-020-03792-y

Facile synthesis and electrochemical study of a ternary hybrid PANI/GNP/MnO_2 as supercapacitor electrode material

Khadija Tul Kubra[1,2] · Atif Javaid[3] · Rehana Sharif[1] · Ghulam Ali[4] · Fauzia Iqbal[5] · Ayesha Salman[1] · Fozia Shaheen[6] · Annam Butt[1] · Faiza Jan Iftikhar[7]

Received: 13 March 2020 / Accepted: 11 June 2020 / Published online: 17 June 2020

Abstract

High-performance electrode materials are required to fulfill the escalating urge of energy storage and the realization of supercapacitors as cutting-edge energy storage devices. This research work presents a facile synthesis of a ternary hybrid material PANI/GNP/MnO_2 using graphene nanoplatelets (GNP), MnO_2 nanowires, and aniline monomer through polymerization for its utility in supercapacitor application. XRD analysis confirms the presence of the individual crystal structures and phases of the constituents and their mutual contribution in a ternary hybrid material. FE-SEM results reveal that PANI nanofibers and MnO_2 nanowires are decorated on the dispersed GNP. N_2 sorption analysis manifests the mesoporous nature of the prepared hybrid. PANI/GNP/MnO_2-based electrode owns 992.6 F/g specific capacitance and 34.5 Wh/kg energy density as well as 51.16% coulombic efficiency and 124.8 W/kg power density at 0.5 A/g. It also exhibits 88.86% coulombic efficiency and 1251 W/kg power density at 5 A/g. The obtained high capacitance, coulombic efficiency, reversibility, and large energy, and power densities make PANI/GNP/MnO_2 ternary hybrid electrode as a promising supercapacitor electrode material.

1 Introduction

Substantial progress in the supercapacitor technology has unfolded many horizons in the field of automotive engineering, complex electronic systems, portable energy storage devices, digital communication systems, magnetic memory devices, and memory backup tools [1–6]. In order to harness simultaneously the high power and energy density of capacitors and batteries, respectively, supercapacitors have come across as a plausible solution that offers to bridge the gap between the two, on account of large surface area and poriferous electrodes along with the utilization of electrolyte solution in their configuration [7]. Other important features to consider are their small size, longer life, fast charging-discharging rate, and cost-efficient [1].

Supercapacitors have three main categories with respect to the working phenomenon, i.e., pseudocapacitors, electric double-layer capacitors (EDLCs), and hybrid supercapacitors. For EDLCs, electric charge is stored by virtue of a direct non-faradaic mechanism developing an EDL which is largely electrostatic in nature. Thus, the charged particles exist at an electrode–electrolyte interface separately by a physical electrostatic attraction. No chemical bond formation or breakage is involved in such a mechanism. The supercapacitors based on porous carbon materials store the charge via this method [8–15]. In contrast, the reversible faradic mechanism takes place in pseudocapacitors by an indirect method, which involves the occurrence of chemical redox reactions for the charge storage [8, 9, 16–18]. The supercapacitors based on redox-active metal oxides function by this mechanism. Whereas, for hybrid supercapacitors, the

✉ Ghulam Ali
ghulamali143@gmail.com

1 Department of Physics, University of Engineering and Technology, Lahore, Pakistan

2 Laser and Optronics Center, University of Engineering and Technology, Lahore, Pakistan

3 Polymer and Process Engineering Department, University of Engineering and Technology, Lahore, Pakistan

4 U.S.-Pakistan Center for Advanced Studies in Energy (USPCASE), National University of Science and Technology (NUST), H-12, Islamabad 44000, Pakistan

5 Department of Physics, University of the Punjab, Lahore, Pakistan

6 Department of Physics, Government College (GC) University, Lahore 54000, Pakistan

7 NUTECH School of Applied Sciences and Humanities, National University of Technology, Islamabad 44000, Pakistan

process of energy storage involves the combination of both electrostatic and redox chemical reactions. Supercapacitors based on redox-active metal oxides and carbon composites work through such a combination.

The synthesis methodology and formulation of electrodes for any supercapacitor are key challenges so far because supercapacitors cannot generate energy density higher than batteries that inhibits its utilization as a major power source [19, 20]. High energy and power along with better structural stability are the crucial parameters that must be considered before synthesizing a supercapacitor electrode material. The exceptional power density is the most significant criterion of any supercapacitor that is connected to the transport mechanism of charges involved [21]. A highly conducting material supplemented by a highly porous structure is mandatory to achieve higher power density, as these parameters reduce polarization, affirm the maximal electrode–electrolyte contact and minimize the ion transport route. All these parameters together enhance transport kinetics. Thus, for enhancing the conductivity of the electrode materials conducting polymers (CPs) [22], carbon-based materials [23, 24] or metals [17], can be employed. To obtain higher energy density, utilization of pseudocapacitive materials such as sulfides/oxides /hydroxide of transition metals, rare earth metal oxides and CPs as promising candidates results in boosting the capacitance and working voltage ramp of the supercapacitor electrode material [25, 26]. Lastly, higher structural strength and stability are necessary for supercapacitor electrode materials to bear mechanical strains during cycling procedure [27].

To obtain improved performance of supercapacitors, major research has been focused on supercapacitor electrode materials synthesized with the redox-active transition metal oxides like RuO_2, Mn_3O_4, NiO, TiO_2, Fe_3O_4, V_2O_5, MoO_3. [28–31] along with rare earth metal oxides Sm_2O_3, Eu_2O_3, CeO_2, Pr_6O_{11} [32–35] and CPs like polythiophene (PT), polypyrrole (PPy), polyethylenedioxythiophene (PEDOT), and polyaniline (PANI) [36]. Moreover, porous large surface area and highly conducting graphene oxide, carbon nanotubes, carbon black, graphite, etc., are composited with the CPs and pseudocapacitive metal oxides to develop the binary nanocomposites [35, 37–40] and ternary hybrids [41, 42] to obtain large conductivity and improved power density. Furthermore, carbonaceous materials prevent the degradation CPs resulting due to charge/discharge cycles leading to their mechanical swelling and contraction [43, 44].

In particular, Das et al. reported a supercapacitor-based novel ternary composite synthesized from MoO_3, polyaniline PANI, and GNP as high energy and power density electrode materials. The ternary composite revealed the remarkably high capacity of 593 F/g at 10 mV/s and also retained 92.4% capacitive retention after 1000 number of cycles [1]. Das et al. prepared composite electrode material (PZG) for its application as a supercapacitor electrode by incorporating polyaniline, zinc acetate, and GNP through oxidative polymerization. PZG composite delivered 688 F/g specific capacitance at 10 mV/s along with 83% capacitive retention after 500 continuous cycles [45]. Moyseowicz et al. presented the fabrication of a composite (PFG) by employing a CP such as PPy, iron oxide Fe_2O_3, and RGO. A hydrothermal reaction was carried out to prepare Fe_2O_3/RGO (FG) composite succeeded by pyrrole polymerization onto FG surface. The resultant ternary composite exhibited 140 F/g at 1 A/g and 93% capacitive retention after 5000 continuous cycles [46]. Jin et al. prepared a ternary composite (GSP) by integrating nanostructured graphene, SnO_2, and PANI using a one-pot procedure. The electrochemical analysis illustrated that the ternary composite (GSP) attained 913.4 F/g at 5 mV/s and kept 90.8% original capacitance over 1000 cycles [41]. Han et al. prepared ternary composites comprised PANI, graphene oxide, and MnO_2 nanorods through a two-step method. A 512 F/g specific capacitance was exhibited by 70% MnO_2 ternary composite along with capacitive retention of about 97% over 5000 numbers of cycles [42]. Thakur et al. developed a ternary composite (PANI/CNT/MoS_2) by in situ polymerization process. A ternary composite comprising 5% MoS_2 in PANI/CNT/MoS_2 achieved 350 F/g specific capacitance at 1.0 A/g with better cycling performance at 10 A/g. The ternary composite exhibited an energy density of 7.77 Wh/kg and a power density of 2140 W/kg [47]. Asen et al. reported a novel V_2O_5/GO/PPy ternary nanocomposite prepared by electrochemical deposition route and investigated its electrochemical performance. This nanocomposite exhibited 750 F/g capacitance at 5 A/g and showed 83% capacity retention over 3000 continual cycles [48]. Alves et al. featured 3D composite of ZrO_2 nanoparticles, PPy and RGO prepared via a simple one-pot chronopotentiometry route. This ternary supercapacitor electrode material delivered specific capacitance of 341 F/g at 0.5 A/g along with better cyclability [49].

In the current study, graphene nanoplatelets (GNP), manganese oxide (MnO_2) nanowires, and polyaniline (PANI) are composited to synthesize a hybrid electrode material for supercapacitor application. The physical advantage behind selecting such materials is that MnO_2 is attributed to pseudocapacitance of the material and enhances energy density. GNP ensures the maximum contact among electrode and electrolyte ions while GNP and PANI together improve the conductivity that consequently increases the power density of hybrid electrode material. Here, the study illustrates the synthesis methodology of PANI/GNP/MnO_2 ternary hybrid electrode material for supercapacitor application via polymerization of aniline with MnO_2 nanowires and GNP in an acidic medium.

2 Experimental work

2.1 Materials

Potassium permanganate ($KMnO_4$, 99–100.5% pure), manganese sulfate monohydrate ($MnSO_4{\cdot}H_2O$, 99–100.5% pure), ethanol (C_2H_5OH, 99.08% pure), cetyltrimethylammonium bromide (CTAB), ammonium persulfate (APS, 98% pure), aniline monomer (99% pure), hydrochloric acid (HCl, 37%) were acquired from Sigma-Aldrich while graphene nanoplatelets (GNP > 99.5% pure, thickness ~ nm, particle size < 2 µm) were supplied by XG Sciences. In all instances, deionized water was used to prepare solutions, nanocomposites and their electrodes.

2.2 Synthesis

2.2.1 MnO_2 nanowires

The hydrothermal route was used to prepare α-MnO_2 nanowires. At first, 0.2 M $KMnO_4$ and 0.125 M $MnSO_4$ solutions were prepared, then both solutions were mixed for 30 min under magnetic stirring which was then transferred to a stainless steel autoclave. This was then kept in an oven at 160 °C for 12 h. After letting it cool, then filtered and rinsed brown precipitates of MnO_2 were dried for 10 h at 70 °C.

2.2.2 PANI/GNP/MnO_2 ternary hybrid

A ternary hybrid PANI/GNP/MnO_2 material was prepared via in situ polymerization of aniline with MnO_2 and GNP [1, 45] as shown in Fig. 1. Initially, 400 ml of 1.5 M HCl solution was prepared. 1.25 g of CTAB as a surfactant was mixed in 250 ml HCl solution under continuous magnetic stirring. Subsequently, 0.1 g of GNP was further added into this solution and allowed to ultrasonicate for about 4 h so that the homogeneous dispersion of stacked layers of GNP was obtained in the presence of the surfactant. Afterwards, this suspension was vigorously stirred for 1 h. Another suspension contained 1.35 g of MnO_2 nanowires in 10 ml deionized water and was poured in the acidic suspension of GNP drop-wise under constant magnetic stirring. Then, 1 ml of aniline monomer was poured in it under ice-cold conditions and stirring was continued for 0.5 h. After that, 2 g of APS was added into the remaining 150 ml of HCl solution in ice-cold conditions. Finally, dropwise addition of ice-chilled APS solution was added into the suspension (GNP, MnO_2, and aniline) under constant stirring maintaining ice-cold conditions. With the addition of APS, the solution instantly turned to a bluish-green color. The resultant mixture was kept overnight under ice-cold conditions. This was followed by filtering and washing of the dark green precipitates with deionized water and ethanol. Finally, the as-obtained precipitates of PANI/GNP/MnO_2 ternary hybrid were dried in an oven at 70 °C for 20 h. The composition (%) of different constituents in the ternary hybrid is PANI:GNP:MnO_2 ≈ 40:4:56.

The PANI/GNP binary hybrid was also synthesized by adopting the same methodology as described above except excluding the MnO_2 addition during the polymerization reaction. A similar procedure was adopted for PANI except for the addition of MnO_2 and GNP in the process of polymerization.

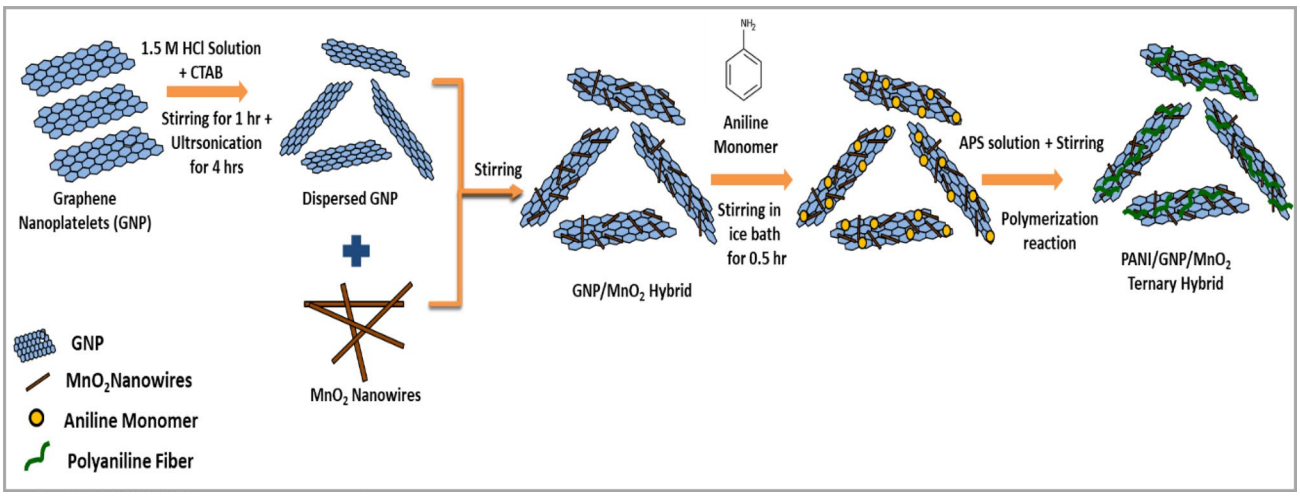

Fig. 1 The synthesis scheme of PANI/GNP/MnO_2 ternary hybrid

3 Characterizations

The surface morphological study was executed through field-emission scanning electron microscopy (FE-SEM, JEORJSM- 6700F). Crystalline phase and structure of each prepared material were examined by X-ray diffraction (XRD, Rigaku Ultima-IV X-ray Diffractometer), from 10° to 70° using Cu Kα characteristic radiation. The surface area and pore profile were studied by NOVA 3200e surface area and pore profile analyzer (Quantachrome, USA).

3.1 Electrochemical analysis and working electrode fabrication

Three-electrode system was employed to perform electrochemical investigation with an electrochemical workstation CHI660C (CH Instruments Inc., USA). Hg/Hg_2SO_4 as a reference, a platinum foil as a counter (auxiliary), and the glassy carbon as a working electrode (WE) were used. The glassy carbon electrode (GCE) was prepared by initially polishing it with alumina slurry. A 2 mg of the synthesized material (PANI, PANI/GNP, or PANI/GNP/MnO_2) and 10 µl Nafion solution were mixed with deionized water through ultrasonication for a few minutes. Subsequently, a solution of 5 µl from the sonicated slurry was drop cast onto the polished GCE and it was allowed to dry at ambient temperature. Additionally, 1 M H_2SO_4 was used as the supporting electrolyte solution during all electrochemical measurements.

4 Results and discussion

4.1 XRD analysis

To examine the crystalline structure of all the synthesized materials, XRD was performed and the XRD results are depicted in Fig. 2. Three typical diffraction peaks for the quasi-crystalline structure of PANI (Fig. 2a) have been observed at 2θ values of 15.2°, 20.9°, and 25.5°, attributing them to its emeraldine salt form [1]. The diffraction peak at $2\theta = 20.9°$ refers to the amorphous PANI peak [50]. Whereas the peak appearing at $2\theta = 25.5°$ is a characteristic PANI peak, that results due to the parallel stacking of polymeric chains of PANI [51, 52]. In XRD pattern for PANI/GNP nanocomposites, diffraction peaks for GNP (hexagonal graphite) at 2θ values of 26.5°, 42.3°, and 44.3° have also been identified along with three characteristic peaks of PANI as demonstrated in Fig. 2b. Moreover, the diffraction peaks at $2\theta = 12.87°$, 18.23°,

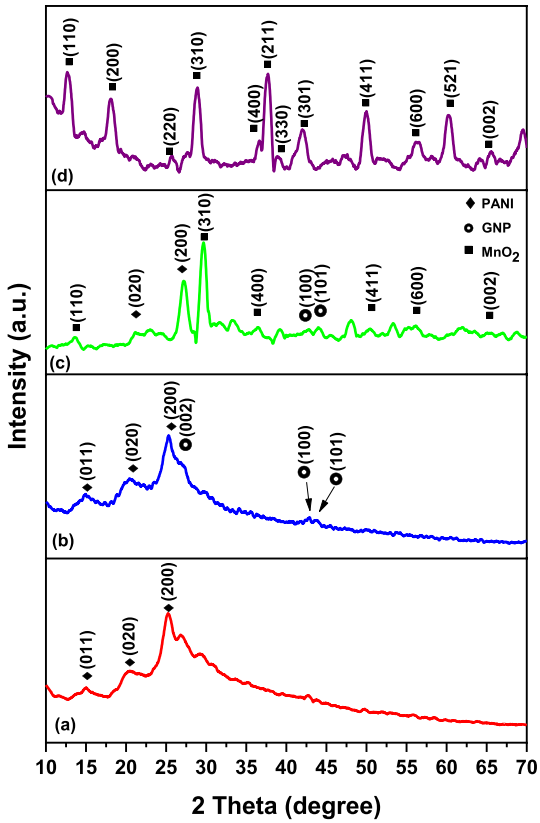

Fig. 2 XRD pattern of **a** pure PANI, **b** PANI/GNP, **c** PANI/GNP/MnO_2, and **d** MnO_2

25.7°, 28.8°, 36.7°, 37.5°, 39.1°, 42.0°, 49.9°, 56.3°, 60.3°, and 65.4° shown in Fig. 2d belong to the tetragonal phase (space group I4/m) of crystalline α-MnO_2, which are well-indexed to standard JCPDS 00-044-0141 [53].

However, along with these peaks of PANI and GNP, the diffraction peaks of tetragonal α-MnO_2 have also been identified in the XRD pattern of PANI/GNP/MnO_2 ternary hybrid as presented in Fig. 2c. This outcome establishes the fact that α-MnO_2 has sustained its phase even in ternary hybrid composite in spite of the polymerization reaction. XRD pattern of PANI/GNP/MnO_2 shows that the corresponding diffraction peaks of constituents become broader and less intense, attributing this to the semi-crystalline behavior of the ternary hybrid that facilitates the fast transference of charge at the electrode–electrolyte boundary [54].

4.2 Field-emission scanning electron microscopy (FE-SEM) analysis

The surface morphological features of the as-prepared materials are presented in Fig. 3. The FE-SEM micrograph of PANI displays a fiber-like appearance (Fig. 3a). The surface morphology of pristine GNP, shown in Fig. 3b, depicts a flake-like structure. Figure 3c shows the irregular attachment

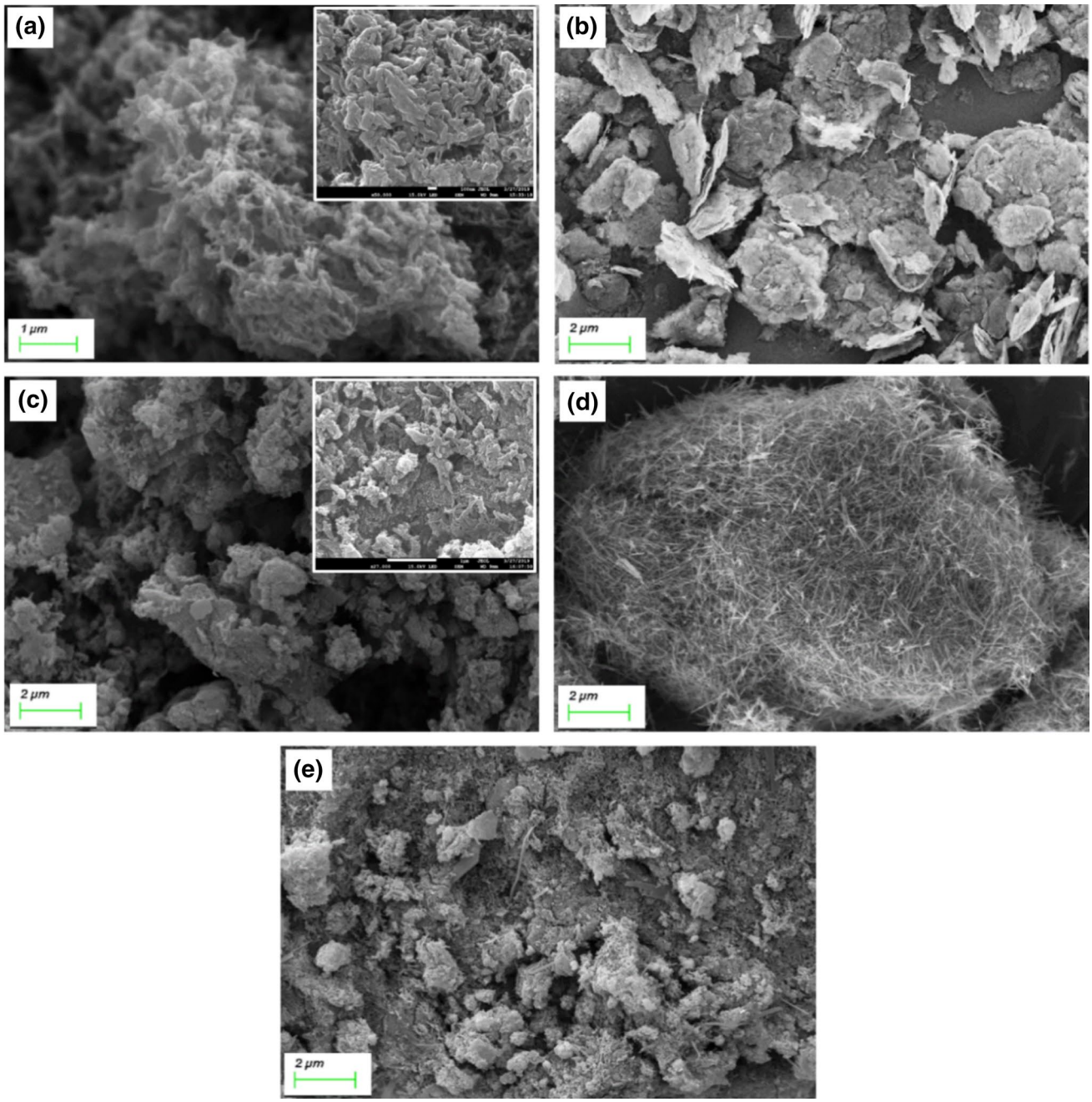

Fig. 3 FE-SEM of **a** PANI, **b** GNP, **c** PANI/GNP, **d** MnO_2, and **e** PANI/GNP/MnO_2

of fibrous PANI over the surface of GNP flakes in PANI/GNP while the hydrothermally synthesized MnO_2 displays a nanowire structure as shown in Fig. 3d.

Furthermore, it is worth noting from FE-SEM micrograph of PANI/GNP/MnO_2 ternary hybrid (Fig. 3e) that MnO_2 nanowires intercalate with GNP flakes and PANI fibers effectively coat on the GNP/MnO_2 nanocomposite. Such a morphology manifests the synergy among the GNP flakes, PANI fibers, and MnO_2 nanowires that expedites the redox-active sites, creates a conductive network and restricts the restacking of GNP. Due to these reasons, such a hybrid material has potential as promising supercapacitor electrodes.

4.3 BET surface area and BJH pore size analysis

The porosity of pristine PANI, PANI/GNP, and PANI/GNP/MnO_2 have been investigated by the nitrogen (N_2) sorption test at 77 K. Figure 4 represents the respective N_2 adsorption–desorption isotherms for the as-prepared materials. It is found that the resultant isotherms belong to type IV isotherm

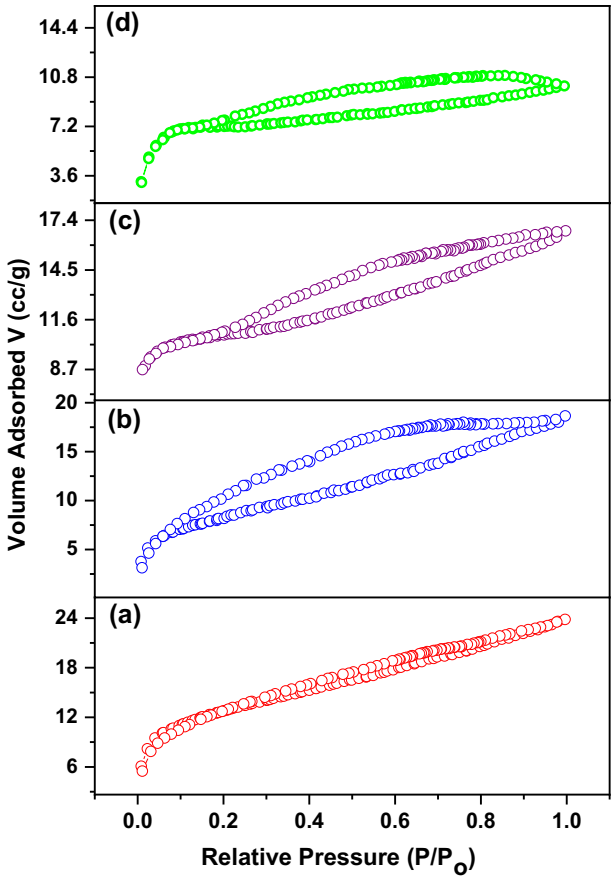

Fig. 4 N_2 sorption isotherms of **a** PANI, **b** PANI/GNP, **c** MnO_2, and **d** PANI/GNP/MnO_2

accompanied by a H3 type hysteresis loop (according to the IUPAC convention) referring to the existence of mesopores in all the adsorbents.

The obvious hysteresis loops are evident in the sorption isotherms of all synthesized materials implying the capillary condensation of nitrogen gas in their mesopores. The estimated BET surface area for PANI, PANI/GNP, MnO_2, and PANI/GNP/MnO_2, are 45.64, 29.92, 36.14, and 22.98 m^2/g respectively. Table 1 tabulates the BJH adsorption pore profile of all the synthesized materials. It is observed that the BJH pore size of all materials lies in the mesoporous range

Table 1 BET surface area, BJH adsorption pore volume, and size of PANI, PANI/GNP, MnO_2, and PANI/GNP/MnO_2

Sample	Surface area (m^2/g)	Cumulative pore volume (cc/g)	Pore size (Å)
PANI	45.64	0.01433	34.96
PANI/GNP	29.92	0.01355	35.02
MnO_2	36.14	0.00883	34.82
PANI/GNP/MnO_2	22.98	0.00723	42.24

that increases the area of electrode/electrolyte interface, needed for superior electrochemical redox reactions. It is seen from Table 1 that pore size increases from pure materials (PANI and MnO_2) to hybrid materials (PANI/GNP and PANI/GNP/MnO_2) with a decrease in BET specific surface area and pore volume. This behavior is manifestation of the internal pore strain caused by the incorporation of GNP and MnO_2 in the pristine materials.

4.4 Electrochemical analysis

4.4.1 CV analysis

Electrochemical redox features of pristine PANI, PANI/GNP, and PANI/GNP/MnO_2 electrodes have been studied through CV analysis, carried out in 1 M H_2SO_4 electrolyte solution over a voltage range of 0.3 V to 0.8 V by applying three-electrode cell configuration. Figure 5 displays the CV curves for the as-synthesized electrodes at a scan rate of 5 mV/s. The asymmetric CV curve for PANI electrode can be ascribed to its redox nature. While the shape of the PANI/GNP CV plot is somewhat rectangular showing the EDLC behavior of GNP. Moreover, the non-rectangular shape of the PANI/GNP/MnO_2 CV curve can be attributed to the combined effect of the pseudocapacitive nature of PANI and MnO_2 along with an EDLC contribution of GNP in this ternary hybrid electrode. Anodic (oxidation), as well as cathodic (reduction) peaks, appear in the positive and negative current regions, respectively.

Figure 5 presents the area under the CV curve for PANI/GNP/MnO_2 electrode that is larger than the pristine PANI and PANI/GNP electrodes which intimate its larger

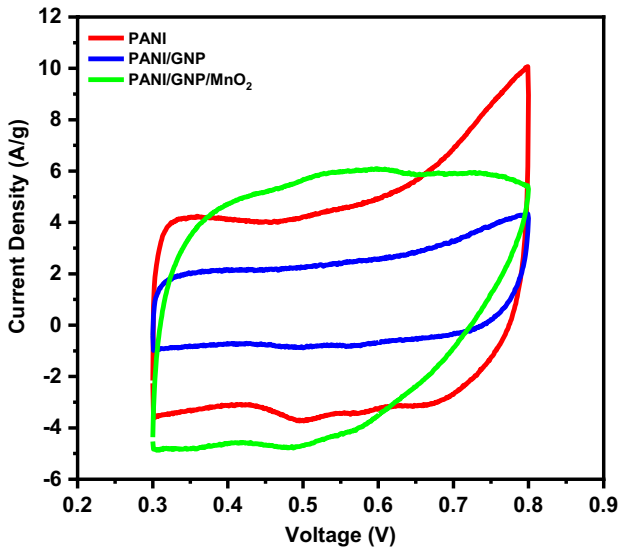

Fig. 5 Cyclic voltammograms for PANI, PANI/GNP, and PANI/GNP/MnO_2 electrodes at 5 mV/s

capacitance [55]. Consequently, PANI/GNP/MnO_2 electrode delivers an exceptional specific capacitance of 871.4 F/g as compared to PANI and PANI/GNP electrodes providing 833.3 and 336.6 F/g specific capacitance, respectively, at a scan rate of 5 mV/s calculated by given Eq. 1 [1, 45].

$$C_s(F/g) = \frac{\int i(V)\mathrm{d}V}{mv\Delta V} \quad (1)$$

where, $\int i(V)dV$ represents the area of CV loop, ΔV is a potential range in volts, v denotes the scan rate in volts/sec and m is the electroactive material mass in grams coated on the surface of the polished GCE.

This enhanced capacitance, i.e., 871.4 F/g at 5 mV/s owned by PANI/GNP/MnO_2 electrode is the influence of mutual impact of all the elements in the ternary hybrid electrode illustrating the facile conduction of electrolyte ions within the network of conductive PANI chains and redox-active MnO_2 nanowires decorated on high surface area GNP. The crystalline nature of α-MnO_2 also exhibits the property of intercalation that significantly contributes to the capacitance of the material by the insertion of cations into the layered structure of α-MnO_2.

Figure 6a–c present the CV curves for all electrodes drawn at different scan rates ranging from 5 to 100 mV/s. It is indicated that CV current response enhances with scan rate for all electrodes, however, the PANI/GNP/MnO_2 electrode displays the higher electrical conductivity and minimum internal resistance in comparison to pristine PANI and PANI/GNP electrodes as it exhibits the maximum current

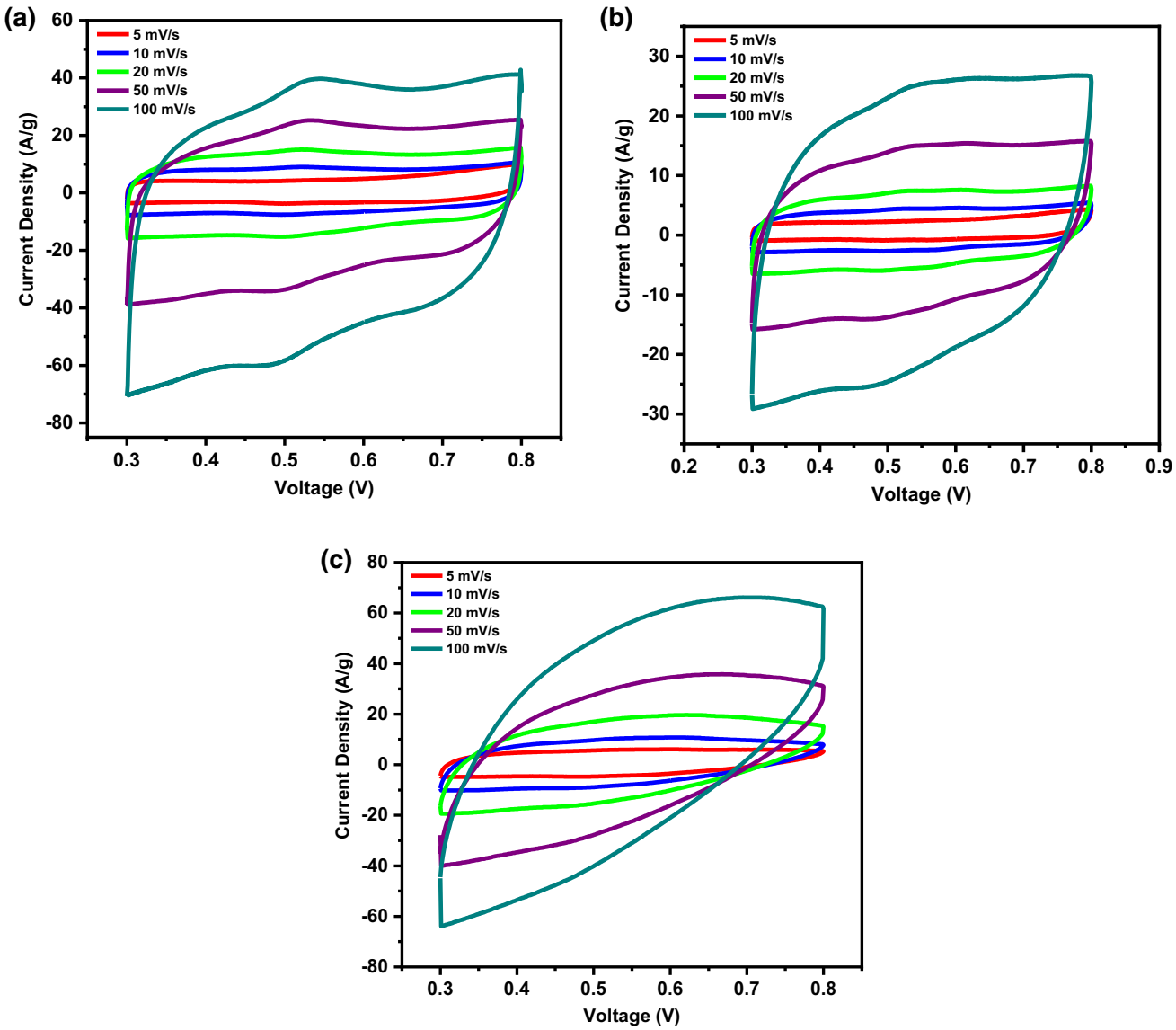

Fig. 6 CV for **a** PANI, **b** PANI/GNP, and **c** PANI/GNP/MnO_2, electrodes at various scan rates

density even at 100 mV/s. The calculated specific capacitances at several scan rates for all the prepared electrodes are shown in Table 2.

Figure 7 demonstrates that the specific capacitance decreases at high scan rates, as at higher scan rates the inner redox-active centers cannot support the redox reactions completely [41]. Conversely, at low scan rates maximum redox-active sites are available for rapid diffusion of electrolyte ions. This rapid diffusion results in enhancing the degree of oxidation–reduction reactions and consequently the value of capacitance goes higher [25, 56].

4.4.2 Galvanostatic charge–discharge (GCD) analysis

The GCD curves for PANI, PANI/GNP, and PANI/GNP/MnO_2 electrodes in 1 M H_2SO_4 as the electrolyte solution were acquired at 0.5 A/g current density. As exhibited in Fig. 8 all the GCD curves present somewhat non-triangular shape, representing the pseudocapacitive nature of MnO_2 and PANI. PANI/GNP/MnO_2 electrode exhibits the highest discharging time than other electrodes.

The specific capacitance of PANI, PANI/GNP, and PANI/GNP/MnO_2 has been noted as 633.3 F/g, 432.3 F/g and 992.6 F/g, respectively, evaluated using Eq. 2 [1, 45].

$$C_s(F/g) = \frac{I\Delta t}{m\Delta V} \tag{2}$$

where I (A) denotes discharging current, Δt (s) discharging time, ΔV(V) operating potential window and m (g) represents the mass of active electrode material immobilized onto the GCE.

The amplified capacitance of mesoporous ternary hybrid electrode is dominated by the charge transfer among the multivalent Mn (+2, + 3, + 4 and +6) element and the doping-dedoping of PANI chains through charge/discharge process. This combination of redox materials produces numerous electroactive centers for redox processes [57]. Additionally, non-faradic capacitance is also contributed by the GNPs. Though, the surface area of ternary hybrid is smaller than the individual materials. Contrarily, PANI/GNP electrode depicts low capacitance in comparison to pure PANI which maybe because of the agglomeration of GNP over PANI

Table 2 Specific capacitances of pristine PANI, PANI/GNP, PANI/GNP/MnO_2 electrodes at various scan rates

Sample	Specific capacitance (F/g)				
	5 mV/s	10 mV/s	20 mV/s	50 mV/s	100 mV/s
PANI	833.3	722.1	633.8	477.2	401.5
PANI/GNP	336.6	315.4	285.4	241.0	206.2
PANI/GNP/MnO_2	871.4	763.0	675.4	486.2	405.5

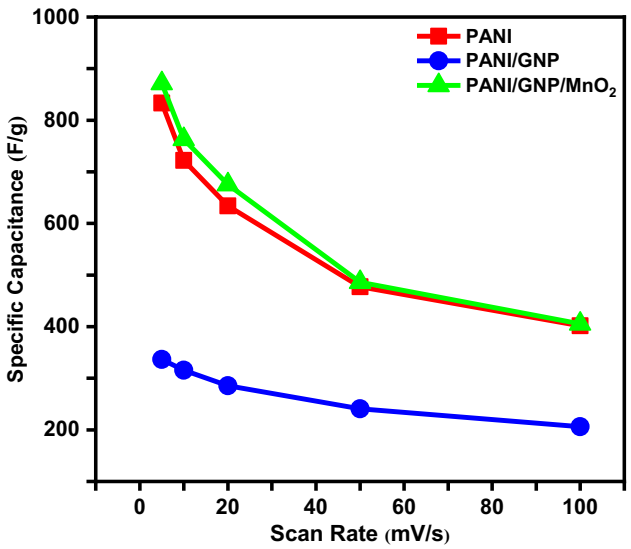

Fig. 7 The relationship between specific capacitance and scan rate

nanofibers causing a reduction in the accessibility of pores to the electrolyte ions for the redox process to happen [47]. In addition, the accumulation of charge at the interface may reduce the specific capacitance as all the carbon material pores are not available for the electrolyte ions [9, 25].

The GCD curves of all electrodes have also been drawn at 0.5, 1, 1.5, 2, and 5 A/g (Fig. 9) to study the influence of high current densities on specific capacitance. Table 3 tabulates the calculated capacitances of the as-prepared electrodes at different current densities.

By virtue of lesser availability of redox-active centers and reduced diffusion of electrolyte ions through the pores of the

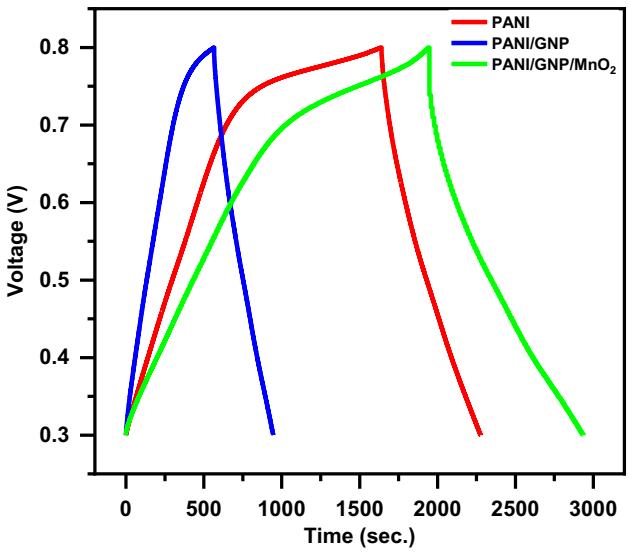

Fig. 8 GCD curves of PANI, PANI/GNP, and PANI/GNP/MnO_2 at 0.5 A/g

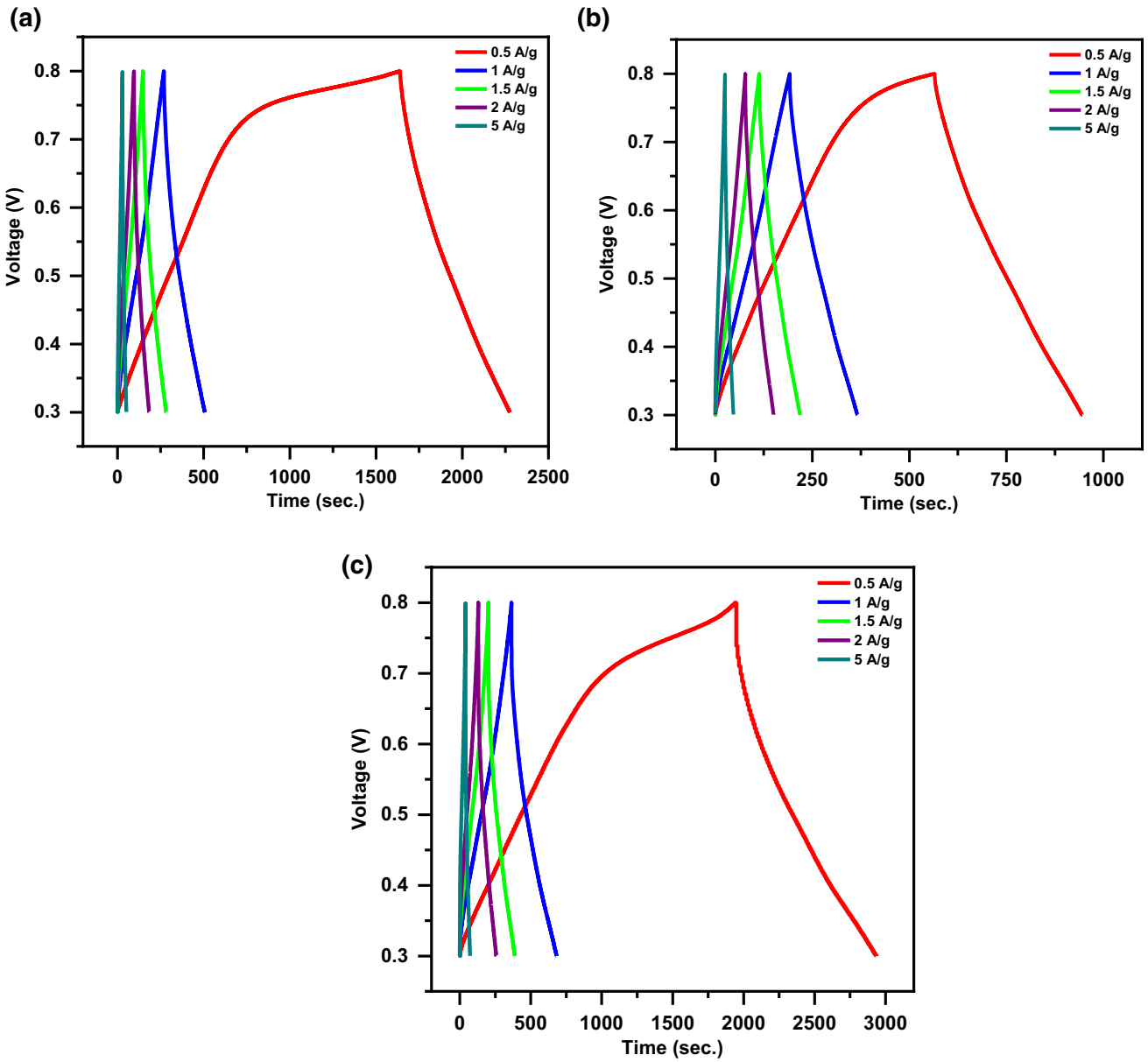

Fig. 9 GCD curves of **a** PANI, **b** PANI/GNP, and **c** PANI/GNP/MnO_2 at various current densities

Table 3 Specific capacitances of pristine PANI, PANI/GNP, PANI/GNP/MnO_2 electrodes at different current densities

Sample	Specific capacitance (F/g)				
	0.5 A/g	1 A/g	1.5 A/g	2 A/g	5 A/g
PANI	633.3	477.1	401.4	352.1	228.5
PANI/GNP	432.3	348.6	312.9	292.8	215.2
PANI/GNP/MnO_2	992.6	635.7	555.2	507.1	316.5

prepared electrodes, their specific capacitances fall with an increase in current density (Fig. 10).

4.4.3 EIS analysis

An EIS study was performed to analyze the capacitive behavior of pristine PANI, PANI/GNP, and PANI/GNP/MnO_2 electrodes over a frequency ranging from 10 mHz to 0.1 MHz and hence interfacial characteristics could be thus delineated. The corresponding Nyquist curves of prepared electrodes are depicted in Fig. 11.

The quantitative values of the ohmic resistance (R_s) for all the prepared electrodes were determined by their

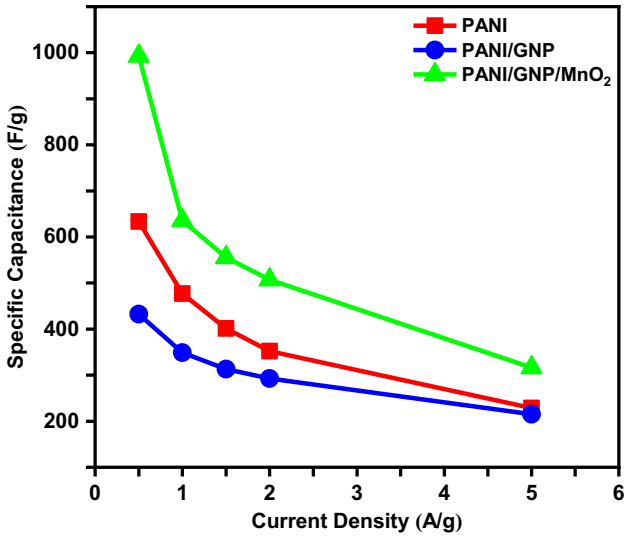

Fig. 10 Relationship between capacitance and current density for PANI, PANI/GNP, PANI/GNP/MnO_2

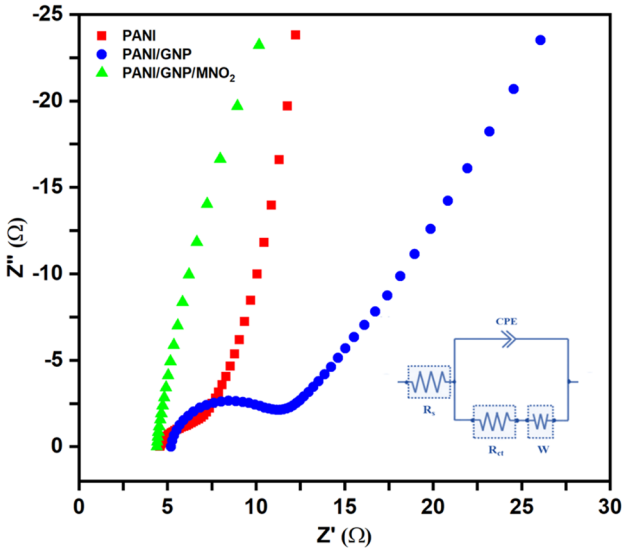

Fig. 11 Nyquist plot for all the prepared electrodes

corresponding non-zero initial semicircle's intercept on the impedance real axis (Z´). The calculated R_s values for pure PANI, PANI/GNP binary hybrid, and PANI/GNP/MnO_2 ternary hybrid are mentioned in Table 4. The PANI/GNP/MnO_2 electrode shows the lowest R_s value, which reflects its highly conductive nature. In the region of high frequency, the semicircular part in all the Nyquist plots correlates to the charge-transfer resistance (R_{ct}). The ternary hybrid electrode has a minimum semicircular diameter than PANI and PANI/GNP electrodes. This relates to the smaller value of R_{ct} (Table 4) for PANI/GNP/MnO_2 electrode at the electrode/electrolyte interface, which implies its good conductive behavior.

Table 4 Estimated ohmic and charge-transfer resistances of prepared electrodes

Sample	R_s (Ω)	R_{ct} (Ω)
PANI	4.6	3.8
PANI/GNP	5.2	6.5
PANI/GNP/MnO_2	4.4	1.6

Table 5 Coulombic efficiencies of pristine PANI, PANI/GNP and PANI/GNP/MNO_2 electrodes at various current densities

Sample	Coulombic efficiency η (%)				
	0.5 A/g	1 A/g	1.5 A/g	2 A/g	5 A/g
PANI	38.86	88.45	90.67	92.66	80.30
PANI/GNP	67.27	91.16	92.97	93.90	85.38
PANI/GNP/MnO_2	51.16	87.37	91.63	98.61	88.86

The nearly vertical profile of PANI/GNP/MnO_2 electrode in the low-frequency region also suggests its lower ion diffusion resistance allowing rapid adsorption of electrolyte ions on the electrode surface, proving its better capacitive nature among the rest of the as-prepared electrodes [48]. These outcomes reveal that PANI/GNP/MnO_2 ternary hybrid electrode exhibits lower ohmic, charge transfer and diffusion resistance and hence good capacitive behavior among all the electrodes investigated in the proposed frequency region due to the synergistic combination of its constituents. Consequently, it is appropriate to use PANI/GNP/MnO_2 ternary hybrid electrode proves to be a robust material for supercapacitor applications.

4.4.4 Coulombic efficiency

Equation 3 [58, 59] is used to calculate the coulombic efficiencies for all prepared electrodes which are summarized in Table 5 at different current densities**.**

$$\eta(\%) = \frac{t_d}{t_c} \times 100 \tag{3}$$

where, t_d and t_c are the discharging and charging times in seconds accordingly.

It is observed that PANI/GNP/MnO_2 electrode holds the highest efficiency of 98.61% as compared to other electrodes at 2 A/g that proves its higher redox reversibility [58].

Furthermore, specific capacitance and coulombic efficiency at varied current density for PANI/GNP/MnO_2 are analyzed as shown in Fig. 12. The coulombic efficiency of the ternary hybrid rises and the capacitance falls with the

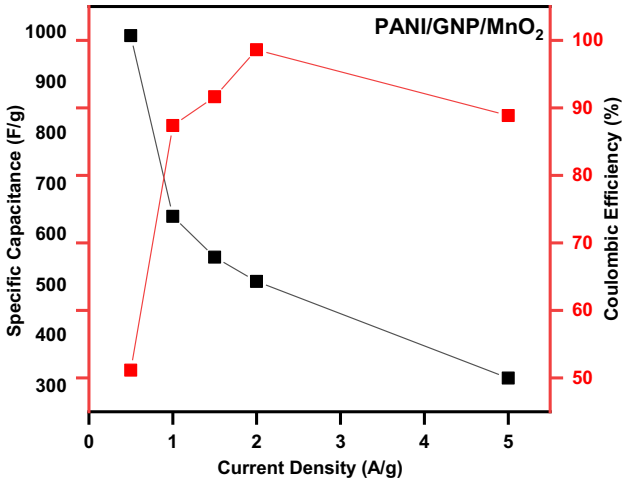

Fig. 12 Specific capacitance and coulombic efficiency as a function of current density for PANI/GNP/MnO_2 electrode

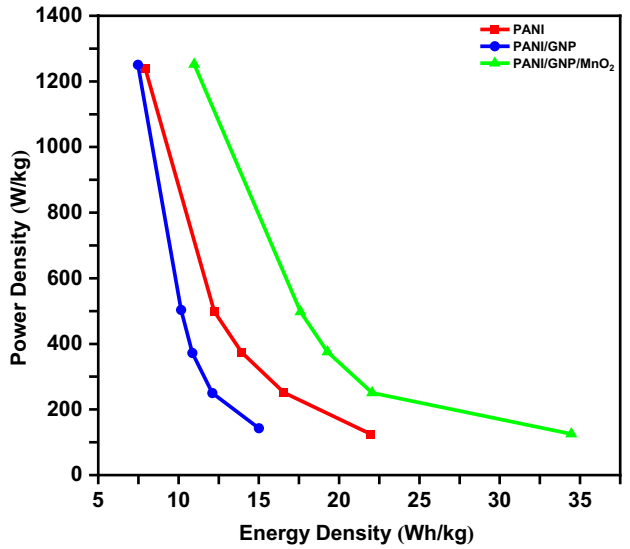

Fig. 13 Ragone plot of all the as-prepared electrodes

upsurge in current density, which can be ascribed to the electrode's inner active sites that are not capable to support the redox reactions at high current densities [60].

4.4.5 Ragone plot

The electrode materials for the supercapacitor must possess substantially large energy and power densities as is shown by the Ragone plot (see Fig. 13). For this reason, the electrochemical analysis of the PANI, PANI/GNP, and PANI/GNP/MnO_2 electrodes has been further carried out by evaluating their energy and power densities from GCD curves using Eqs. 4 and 5 [34].

$$E(Wh/kg) = \frac{1}{7.2} C_s(\Delta V)^2 \tag{4}$$

$$P(W/kg) = 3600 \frac{E}{\Delta t} \tag{5}$$

where C_s (F/g), Δt (s) and ΔV (V) denotes the specific capacitance, discharging time and potential ramp, respectively, obtained through GCD results.

At 0.5 A/g, PANI/GNP/MnO_2 electrode exhibits an energy density = 34.5 Wh/kg and power density = 125 W/kg in comparison to 21.9 Wh/kg and 15.1 Wh/kg energy densities along with 124 W/kg and 142 W/kg power densities for PANI and PANI/GNP electrodes, respectively. This value of energy density is higher than the individual, binary and ternary hybrid electrodes as reported in literature [47, 61–64]. Moreover, PANI/GNP/MnO_2 electrode also exhibits 11 Wh/kg energy density with significantly higher power density of 1251 W/kg at 5 A/g as compared to other electrodes. These results reflect excellent synergy among pseudocapacitive MnO_2 nanowires, PANI nanofibers and charge transferring conducting GNP of the ternary hybrid electrode that promotes deep spreading and intercalation of the electrolyte ions into the electrode and hence influence the excellent charge storage capacity.

5 Conclusions

A ternary hybrid PANI/GNP/MnO_2 has been prepared through in situ polymerization of aniline with MnO_2 nanowires and GNP. XRD results confirm the emeraldine salt form of PANI, hexagonal graphite structure of GNP and tetragonal phase of crystalline α-MnO_2 with broader and less intense diffraction peaks of all the phases in PANI/GNP/MnO_2. FE-SEM image reflects that PANI nanofibers and MnO_2 nanowires are decorated on the dispersed flakes of GNP. Furthermore, PANI/GNP/MnO_2-based electrode also exhibits a larger capacitance of about 992.6 F/g than 633.3 F/g for pristine PANI electrode and 432.3 F/g for PANI/GNP binary hybrid electrode at 0.5 A/g. The electrode also possesses lower ohmic, charge transfer and diffusion resistances and hence shows good capacitive behavior in the investigated frequency region due to the synergistic combination of its constituents. Moreover, it retains a coulombic efficiency of about 88.86% at 5 A/g. The electrode also exhibits 34.5 Wh/kg and 11 Wh/kg energy density as well as 125 W/kg and 1251 W/kg power density at 0.5 A/g and 5 A/g, correspondingly, higher than any other of the electrodes employed in this work. Consequently, it is appropriate to use a PANI/GNP/MnO_2 ternary hybrid as a material for supercapacitor electrodes owing to its high pseudocapacitance, rate

capability, coulombic efficiency, reversibility, and appropriate energy, and power density.

Acknowledgement This research was supported by the University of Engineering and Technology (UET), Lahore, Pakistan.

References

1. A.K. Das, S.K. Karan, B.B. Khatua, Electrochim. Acta **180**, 1 (2015)
2. J.S. Shayeh, A. Ehsani, M.R. Ganjali, P. Norouzi, B. Jaleh, Appl. Surf. Sci. **353**, 594 (2015)
3. L. Kouchachvili, W. Yaïci, E. Entchev, J. Power Sources **374**, 237 (2018)
4. A.S. Lemine, M.M. Zagho, T.M. Altahtamouni, N. Bensalah, Int. J. Energy Res. **42**, 4284 (2018)
5. Y. He, W. Chen, X. Li, Z. Zhang, J. Fu, C. Zhao, ACS Nano **7**, 174 (2013)
6. P. Simon, Y. Gogotsi, Nat. Mater. **7**, 845 (2008)
7. P. Sharma, T.S. Bhatti, Energy Convers. Manage. **51**, 2901 (2010)
8. S.M. Chen, R. Ramachandran, V. Mani, R. Saraswathi, Int. J. Electrochem. Sci. **9**, 4072 (2014)
9. Y. Zhang, H. Feng, X. Wu, L. Wang, A. Zhang, T. Xia, Int. J. Hydrog. Energy **34**, 4889 (2009)
10. E. Frackowiak, Q. Abbas, F. Beguin, J. Energy Chem. **22**, 226 (2013)
11. M. Nasibi, M.A. Golozar, G. Rashed, Mater. Lett. **91**, 323 (2013)
12. L. Yang, L.R. Hou, Y.W. Zhang, C.Z. Yuan, Mater. Lett. **97**, 97 (2013)
13. J.P. Zheng, P.C. Goonetilleke, C.M. Pettit, D. Roy, Talanta **81**, 1045 (2010)
14. D. Qu, J. Power Sources **109**, 403 (2002)
15. H. Shen, E. Liu, X. Xiang, Z. Huang, Y. Tian, Y. Wu, Mater. Res. Bull. **47**, 662 (2012)
16. J. Jiang, A. Kucernak, Electrochim. Acta **47**, 2381 (2002)
17. X. Lang, A. Hirata, T. Fujita, M. Chen, Nat. Nanotechnol. **6**, 232 (2011)
18. H. Gomez, M.K. Ram, F. Alvi, P. Villalba, E. Stefanakos, A. Kumar, J. Power Sources **196**, 4102 (2011)
19. X. Xia, D. Chao, Z. Fan, C. Guan, X. Cao, H. Zhang et al., Nano Lett. **14**, 1651 (2014)
20. G.X. Pan, X.H. Xia, F. Cao, J. Chen, P.S. Tang, Y.J. Zhang et al., Electrochim. Acta **133**, 522 (2014)
21. C. Liu, F. Li, L.P. Ma, H.M. Cheng, Adv. Energy Mater. **22**, E28 (2010)
22. Q. Wu, Y. Xu, Z. Yao, A. Liu, G. Sh, ACS Nano **4**, 1963 (2010)
23. S.W. Lee, J. Kim, S. Chen, P.T. Hammond, Y. Shao-Horn, ACS Nano **4**, 3889 (2010)
24. J. Yan, Z. Fan, W. Sun, G. Ning, T. Wei, Q. Zhang et al., Adv. Funct. Mater. **22**, 2632 (2012)
25. G. Wang, L. Zhang, J. Zhang, Chem. Soc. Rev. **41**, 797 (2012)
26. K. Wang, H. Wu, Y. Meng, Z. Wei, Small **10**, 14 (2014)
27. C. Guan, X. Li, Z. Wang, X. Cao, C. Soci, H. Zhang et al., Adv. Mater. **24**, 4186 (2012)
28. G. Lee, Y. Cheng, C.V. Varanasi, J. Liu, J. Phys. Chem. C **118**, 2281 (2014)
29. M. Sathiya, A.S. Prakash, K. Ramesha, J.-M. Tarascon, A.K. Shukla, J. Am. Chem. Soc. **133**, 16291 (2011)
30. X.-C. Dong, H. Xu, X.-W. Wang, Y.-X. Huang, M.B. Chan-Park, H. Zhang et al., ACS Nano **6**, 3206 (2012)
31. W. Li, G. Li, J. Sun, R. Zou, K. Xu, Y. Sun et al., Nanoscale **5**, 2901 (2013)
32. G.P. Ojha, B. Pant, S.-J. Park, M. Park, H.-Y. Kim, J. Colloid Interface Sci. **494**, 338 (2017)
33. H. Zhang, J. Gu, J. Tong, Y. Hu, B. Guan, B. Hu et al., Chem. Eng. J. **286**, 139 (2016)
34. X. Zhang, M. He, P. He, H. Liu, H. Bai, J. Chen et al., Appl. Surf. Sci. **426**, 933 (2017)
35. K.T. Kubra, A. Javaid, B. Patil, R. Sharif, A. Salman, S. Shahzadi et al., Ceram. Int. **45**, 6819 (2019)
36. P. Liu, Y. Wang, X. Wang, C. Yang, Y. Yi, J. Nanoparticle Res. **14**, 1 (2012)
37. S. Ahmed, M. Rafat, Mater. Res. Express **5**, 015507 (2018)
38. S. Ahmed, M. Rafat, Mater. Res. Express **5**, 035512 (2018)
39. S. Ahmed, M. Rafat, M.K. Singh, S. Hashmi, Nanotechnology **29**, 395401 (2018)
40. K.T. Kubra, R. Sharif, B. Patil, A. Javaid, S. Shahzadi, A. Salman et al., J. Alloys Compd. **815**, 152104 (2020)
41. Y. Jin, M. Jia, Coll. Surf. A **464**, 17 (2015)
42. G. Han, Y. Liu, L. Zhang, E. Kan, S. Zhang, J. Tang et al., Sci. Rep. **4**, 1 (2014)
43. N.A. Kumar, H.-J. Choi, Y.R. Shin, D.W. Chang, L. Dai, J.-B. Baek, ACS Nano **6**, 1715 (2012)
44. Y. Yan, Q. Cheng, V. Pavlinek, P. Saha, C. Lia, Electrochim. Acta **71**, 27 (2012)
45. A.K. Das, S. Maiti, B.B. Khatua, J. Electroanal. Chem. **739**, 10 (2015)
46. A. Moyseowicz, A. Sliwak, E. Miniach, G. Gryglewicz, Composites B **109**, 23 (2017)
47. A.K. Thakur, A.B. Deshmukh, R.B. Choudhary, I. Karbhal, M. Majumder, M.V. Shelke, Mater. Sci. Eng. B **223**, 24 (2017)
48. P. Asen, S. Shahrokhian, A.I. Zad, Int. J. Hydrog. Energy **42**, 21073 (2017)
49. A.P.P. Alves, R. Koizumi, A. Samanta, L.D. Machado, A.K. Singh, D.S. Galvao et al., Nano Energy **31**, 225 (2017)
50. H. Farrokhzad, T. Van Gerven, B. Van der Bruggen, Eur. Polym. J. **49**, 3234 (2013)
51. D.K. Bandgar, G.D. Khuspe, R.C. Pawar, C.S. Lee, V.B. Patil, Appl. Nanosci. **4**, 27 (2014)
52. F. Cheng, W. Tang, C. Li, J. Chen, H. Liu, P. Shen et al., Chemi: Eur. J. **12**, 3082 (2006)
53. W.-C. Peng, S.-B. Wang, X.-Y. Li, Sep. Purif. Technol. **163**, 15 (2016)
54. C. Liu, H. Sun, J. Qian, Z. Chen, F. Chen, S. Liu et al., J. Alloys Compd. **722**, 54 (2017)
55. W. Fan, C. Zhang, W.W. Tjiu, K.P. Pramoda, C. He, T. Liu, A.C.S. Appl, Mater. Interfaces **5**, 3382 (2013)
56. M.D. Stoller, S. Park, Y. Zhu, J. An, R.S. Ruoff, Nano Lett. **8**, 3498 (2008)
57. F. Meng, X. Yan, Y. Zhu, P. Si, Nanoscale Res. Lett. **8**, 179 (2013)
58. M. Majumder, R.B. Choudhary, A.K. Thakur, I. Karbhal, RSC Adv. **7**, 20037 (2017)
59. M. Majumder, R.B. Choudhary, A.K. Thakur, C.S. Rout, G. Gupta, New J. Chem. **42**, 5295 (2018)
60. S.R. Ede, S. Anantharaj, K. Kumaran, S. Mishra, S. Kundu, RSC Adv. **7**, 5898 (2017)
61. H. Chen, B. Zhang, F. Li, M. Kuang, M. Huang, Y. Yang et al., Electrochim. Acta **187**, 488 (2016)
62. F. Li, Y.X. Zhang, M. Huang, Y. Xing, L.L. Zhang, Electrochim. Acta **154**, 329 (2015)
63. X. Liu, P. Shang, Y. Zhang, X. Wang, Z. Fan, B. Wang et al., J. Mater. Chem. A **2**, 15273 (2014)
64. L. Zhang, D. Huang, N. Hu, C. Yang, M. Li, H. Wei et al., J. Power Sources **342**, 1 (2017)